Accurate Measurements of Aerosol Hygroscopic Growth

Over a Wide Range in Relative Humidity

Grazia Rovelli,[1,2] Rachael E.H. Miles,[1] Jonathan P. Reid,[1,] and Simon L. Clegg[3]*

[1] School of Chemistry, University of Bristol, Bristol, BS8 1TS, UK

[2] Department of Earth and Environmental Sciences, University of Milano-Bicocca, 20124 Milan, Italy

[3] School of Environmental Sciences, University of East Anglia, Norwich NR4 7TJ, UK

Abstract

Using a comparative evaporation kinetics approach, we describe a new and accurate method for determining the equilibrium hygroscopic growth of aerosol droplets. The time-evolving size of an aqueous droplet, as it evaporates to a steady size and composition that is in equilibrium with the gas phase relative humidity, is used to determine the time-dependent mass flux of water, yielding information on the vapour pressure of water above the droplet surface at every instant in time. Accurate characterization of the gas phase relative humidity is provided from a control measurement of the evaporation profile of a droplet of know equilibrium properties, either a pure water droplet or a sodium chloride droplet. In combination, and by comparison with simulations that account for both the heat and mass transport governing the droplet evaporation kinetics, these measurements allow accurate retrieval of the equilibrium properties of the solution droplet (i.e. the variations with water activity in the mass fraction of solute, diameter growth factor, osmotic coefficient or number of water molecules per solute molecule). Hygroscopicity measurements can be made over a wide range in water activity (from >0.99 to, in principle, <0.05) on timescales of <10 s for droplets containing involatile or volatile solutes. The approach is benchmarked for binary and ternary inorganic solution aerosols with typical uncertainties in water activity of <±0.2 % at water activities >0.9 and ~±1 % below 80 % RH, and maximum uncertainties in diameter growth factor of ±0.7 %. For all of the inorganic systems examined, the time-dependent data are consistent with large values of the mass accommodation (or evaporation) coefficient (>0.1).

Corresponding author: Jonathan P. Reid, j.p.reid@bristol.ac.uk, telephone +44 117 331 7388.

1. INTRODUCTION

Quantifying the equilibrium hygroscopic growth of aerosol is important for understanding the liquid water content and size distributions of atmospheric aerosol and for modelling their optical properties, for predicting cloud droplet number and size distribution following the activation of cloud condensation nuclei (CCN), and for determining the partitioning of semi-volatile organic compounds (SVOCs) in the condensed aerosol phase.[1,2] The capacity for aerosols to absorb water can also influence their deposition in the respiratory track on inhalation, potentially influencing the impact of aerosols on health.[3] The uncertainties in understanding these processes provide an incentive to improve the characterisation of aerosol hygroscopicity. As an example, cloud parcel models have shown that the cloud droplet number can vary by as much as 50% depending on the strength of the assumed hygroscopic growth as saturation is approached.[4]

Rigorous thermodynamic models for calculating the hygroscopic response of mixed component aerosol have been developed based on bulk phase and aerosol phase measurements of the equilibrium response of binary solutions of a single solute and water.[5,6] When combined with treatments of solution density and surface tension, accurate predictions of the variation in equilibrium particle size with relative humidity are possible.[7,8] To represent the equilibrium properties of solutions containing the myriad of potential organic compounds found in the atmosphere, it is often necessary to resort to functional group activity models which require consideration of the interactions between electrolytes and organic species.[9,10] However, there is also a requirement to provide models of hygroscopic growth that are tractable in computational models of atmospheric chemistry, radiative transfer and climate models. To achieve this, models such as κ-Köhler theory have been developed to represent the hygroscopicity of aerosol particles using a single value of κ, with a higher value representing more hygroscopic aerosol (>0.5 for ammonium sulphate and sodium chloride) and a lower value representing less hygroscopic aerosol (<0.05 for insoluble fatty acids).[11,12] Measurements of κ have been made for aerosols varying in complexity from binary component solution aerosol through to the complex inorganic-aqueous mixtures found in the atmosphere.[13–15]

At a fundamental level, both the thermodynamic factors governing hygroscopic growth and the kinetics of condensation must be better quantified in order to represent the aerosol microphysics under-pinning the partitioning of water between the gas and particle phases. A number of significant uncertainties must be addressed to improve the microphysical description of water partitioning. There can be significant differences

2

between hygroscopic growth measurements made on different instruments.[16] Further, estimates of the critical supersaturation for CCN activation inferred from κ values determined from measurements under sub-saturated conditions are often inconsistent with values determined directly.[16,17] The gas-particle partitioning of volatile organic compounds (VOCs) and SVOCs, and co-condensation with water during CCN activation is poorly constrained and has been largely ignored, not only effecting predictions of particle growth in the atmosphere but introducing ambiguity into measurements of hygroscopic growth.[2] Although the molecular complexity of secondary organic aerosol (SOA) precludes an accurate treatment of hygroscopic growth that explicitly accounts for each compound individually, empirical correlations that seek to exploit dependencies on average measures of composition (e.g. the variation of κ with O:C ratio) are often poorly defined and, at best, appropriate only for specific SOA precursors and environmental conditions.[13–15] The slow deliquescence and low solubility of some organic components present challenges in interpreting measurements of hygroscopic growth.[18] Liquid-liquid phase separation into internal mixtures of hydrophobic and hydrophilic phases in mixed component aerosol remains a challenge in predicting equilibrium properties.[19,20] The extent of the depression of surface tension by surface active organic components and the interplay of surface and bulk partitioning in determining the critical supersaturation remains difficult to resolve.[21,22] Finally, the kinetics of water, VOC and SVOC condensation are often poorly determined with few quantitative measurements of the mass accommodation coefficients of organic species in particular.[23–25]

To address the challenges in quantifying hygroscopicity for aerosols of complex composition, refinements in laboratory and field instrumentation, and improved frameworks for representing hygroscopicity, are required.[26,27] Hygroscopic growth measurements must be made up to water activities close to the dilute limit, ideally as high as 0.999. Such high water activities (a_w) are required for measurements to be directly relevant to CCN activation[28] and to place tighter constraints on the equilibrium solution compositions required to underpin the development of predictive models.[29] Building on our previous preliminary report,[32] we present here a more general and wide ranging characterisation of a new method for deriving hygroscopic growth curves for coarse mode particles over a wide water activity range (in principle from dry conditions to >0.999). We concentrate on aerosol droplets of well-known composition and containing well-characterised electrolytes in order to benchmark the technique. Growth curve measurements can be determined rapidly and accurately, potentially opening up the possibility of mapping hygroscopic response for a large number of organic

components of SOA and, indeed, complex mixtures and SOA samples directly. In Section 2 we review the experimental technique and the analyses methods used before presenting measurements of hygroscopic growth for binary solutions of sodium chloride, ammonium sulphate, sodium sulphate and sodium nitrate in Section 3. We also consider the accuracy of the approach by exploring the ability of the instrument to resolve small changes in hygroscopic growth for mixed-salt containing aerosol droplets.

2. EXPERIMENTAL

Comparative kinetics measurements for the quantification of the hygroscopicity of aerosols using the cylindrical electrodynamic balance (EDB) experimental setup have been described in previous publications.[32–34] In this section, an overview of the instrument and of the determination of hygroscopic properties from measurements on multiple droplets is presented, extending our previous work over a wider range in water activity. The adopted treatments for refractive index and density are also introduced.

2.1 The Cylindrical EDB

The EDB technique allows the levitation of a single charged aerosol droplet inside an electrical field. Single droplets are generated on-demand from a solution with known initial concentration by applying a pulse voltage to the filled reservoir of a microdispenser (Microfab MJ-ABP-01), placed just outside one of the walls of the EDB chamber. In between droplet generation events, a smaller constant pulse voltage is applied to the microdispenser in order to continuously flush some solution through its tip, thus assuring that no evaporation of solvent and no variation of the solution concentration can occur from measurement to measurement. The initial radius of the droplets once trapped varies from about 18 to 25 μm. Before entering the trapping chamber, a net charge is imparted to every droplet by means of a high-voltage induction electrode. Within 100 ms of its generation, the droplet is tightly confined in the centre of the electrodynamic field inside the EDB chamber. An AC signal is applied to the cylindrical electrodes and a DC offset is superimposed, in order to balance the gravitational and drag forces on the trapped droplet. The cylindrical configuration of the electrodes results in a steep gradient in the potential in the trapping region, guaranteeing a strong confinement of the droplets,[35] with little harmonic oscillation in the position of the particle that is characteristic of other electrode configurations.

The droplet is confined within a gas flow, which results from the mixing of wet and dry nitrogen flows. It is possible to change the ratio between these two flows by means of mass flow controllers (MKS 1179A) and this allows the control of the relative humidity (RH) of the gas phase that surrounds the droplet. The temperature of the chamber is controlled by recirculating a mixture of water and ethylene glycol (50% v/v) from a thermostatic water bath (Julabo, F32-HE) through the lid and the bottom of the chamber. The accessible temperature range is -25 to 50 °C. In this study all the measurements were performed at 20 °C.

The trapped droplet is illuminated by light from a green laser (λ = 532 nm). The resulting elastic scattering pattern is collected every 10 ms over a range of solid angles centred at 45° by means of a CCD camera and is used to determine the radius of the droplet with the simplified geometrical optics approximation approach,[36] using Equation (1):

$$a = \frac{\lambda}{\Delta\theta}\left(\cos(\theta/2) + \frac{m\sin(\theta/2)}{\sqrt{1 + m^2 - 2m\cos(\theta/2)}}\right)^{-1} \tag{1}$$

where a is the droplet radius, λ is the incident wavelength, θ is the central viewing angle, $\Delta\theta$ is the angular separation between the fringes in the scattering pattern and m is the refractive index of the droplet. The error associated with the radius determination with this approach is ±100 nm.

The refractive index of the evaporating droplets is not constant because the solute concentration increases as water evaporates. This variation of the refractive index with time must be taken into account for an accurate determination of the droplet radii. At first, during the data acquisition, m is set constant at 1.335, the value for pure water at 532 nm. In a post-acquisition analysis step, the radii data are corrected by taking into account the variation of the refractive index with mass fraction of solute (*mfs*) by applying the molar refraction mixing rule,[37] which has been demonstrated to be the best mixing rule to describe the refractive index for a number of inorganic systems.[38] The molar refraction (R) of a component i is defined as:

$$R_i = \frac{(m_i^2 - 1)M_i}{(m_i^2 + 2)\rho_i} = \frac{(m_i^2 - 1)V_i}{(m_i^2 + 2)} \tag{2}$$

where M_i is the compound's molecular mass and ρ_i is its pure melt density. The ratio of molecular mass to liquid density is equivalent to the molar volume of pure i, V_i. The molar refraction for the solution, R, is the

sum of the molar refractions of each component, including all solutes and water, weighted by their mole fractions (x_i):

$$R = \sum_i x_i R_i \tag{3}$$

In this study, the variation in solution densities with mass fraction of solute and the pure solute melt densities are taken from the work of Clegg and Wexler.[39] The melt densities are extrapolations from high temperature measurements compiled and evaluated by Janz.[40] For ease of data processing, the density data are represented as a function of the square root of the mass fraction of solute ($mfs^{0.5}$) and fitted with a polynomial curve (order ranging from 4th to 7th) so that the residual from the fit is <0.005 g.cm^{-3} across the whole mfs range. This density dependence is then used to constrain a least-squares fit of the tabulated data of solution refractive index for solute concentrations below the solubility limit,[41] to the functional dependence of the molar refraction mixing rule. The only fit parameter is the value of the pure component refractive index of the molten salt. From this fit, the value of the refractive index of the solution, m, at any solute concentration can then be found from Equation (4) by solving for m using the mfs, the estimated density of the solution at this composition ρ, a mole fraction weighted molecular mass M, and the estimated molar refraction of the solution.

$$R = \frac{(m^2 - 1)M}{(m^2 + 2)\rho} \tag{4}$$

The procedure used to take into account the variation in refractive index during the evaporation is the following. There is a time-period (~0.1 s) between droplet generation and the first determination of size when the droplet is in transit into the trapping region.[32,33] Thus, the initial size of the droplet is estimated with a linear extrapolation of the a^2 vs. time plot to $t = 0$ s; the initial solute mass fraction and density of solute solution at $t = 0$ s and at this droplet size are known from the prepared solution.[33] The elastic light scattering data are first analysed with $m = 1.335$ to yield an initial estimate of the variation in radius with time, also providing a first estimate of the variation of the solute concentration and of the solution density during the evaporation. A set of corrected refractive indices for the droplet solution at every time-step is then calculated based on the change in size using the molar refraction mixing rule (Equations 2-4). These corrected refractive indices at each time

point are then used to fit a new set of corrected radii with Equation 1. This procedure is repeated for the new set of corrected radii until the refractive indices and radii values converge, typically after 2-3 iterations.

One key feature of this experimental setup is the presence of two microdispensers that can be operated sequentially, thus allowing the generation of aerosol droplets with different chemical compositions in rapid succession. This feature allows comparative kinetics measurements, which consist of levitating a sequence of droplet pairs; one probe droplet (either water or a well-characterised salt solution, such as NaCl), followed by one sample droplet containing the solution of interest. Typically, these kind of comparative kinetic measurements consist of a series of at least ten pairs of probe and sample droplets. The evaporation kinetics of the probe droplets (when water) or their equilibrated size (when aqueous NaCl) are used to determine the gas phase RH, which is key information for the interpretation of the evaporation profile of the unknown sample droplet, as will be discussed in Sections 2.2 and 2.3.

2.2 Modelling Aerosol Droplet Evaporation Kinetics

The mass and heat transport equations from Kulmala and coworkers[42] can be used to model the evaporation and condensation kinetics of water or other volatile species from/to aerosol droplets. For the evaporation case, the mass flux from the droplet (I) depends on the concentration gradient of the evaporating species (water in this work) from the droplet surface to infinite distance. We have considered the influence of droplet charge on evaporation rates in previous work,[32] showing it to have negligible impact at the imbalance of positive and negative ions induced in the droplets studied in these experiments.[44] The mass transfer enhancement resulting from the flowing gas surrounding the droplet is accounted for by the inclusion of a Sherwood number (Sh) scaling of the mass flux.[33,43] The thermophysical parameters that appear in the mass flux treatment and their uncertainties have been thoroughly discussed in previous publications.[32,34,45,46] The resulting expression for the mass flux is the following:

$$I = -2Sh\pi a(S_\infty - a_w)\left[\frac{RT_\infty}{M\beta_M Dp^0 T_\infty A} + \frac{a_w L^2 M}{KR\beta_T T_\infty^2}\right]^{-1} \tag{5}$$

where Sh is the Sherwood number, S_∞ is the saturation ratio of water in the surrounding gas phase (also referred to as RH in this work), a_w is the water activity in the droplet solution, R is the ideal gas constant, T_∞

is the gas phase temperature, L is the latent heat of vaporisation, and M is the molar mass of water. β_M and β_T are the transition correction factors for mass and heat respectively; these corrections are very small for the coarse mode droplet sizes considered here and this will be demonstrated when we consider the sensitivity of the thermodynamic measurement to the value of the mass accommodation coefficient. D is the diffusion coefficient of water in the gas phase, p^0 is the saturation vapour pressure of water, A is the Stefan flow correction and K is the thermal conductivity of the gas phase.

As an example of the data acquired during droplet evaporation, a series of seven $(NH_4)_2SO_4$ solution droplets evaporating into different RHs at 20°C are shown in Figure 1A over the range from 50 % to 85 % RH. The initial mass fraction of the starting solution was 0.05 and the initial radii of the seven different droplets varied from 23.0 μm to 23.3 μm. The total amount of water that evaporates from each droplet depends on the gas phase RH and the final equilibrated radius is such that the a_w in the droplet matches the RH in the surrounding gas phase. The evaporation rate increases with decreasing RH since the mass flux is proportional to the difference between the solution water activity and the RH (Equation (5)). As shown in Figure 1B, the mass flux is at its highest value for every droplet at the beginning of the evaporation because $S_\infty - a_w$ is at its maximum. Over time, the evaporation slows down and the mass flux decreases until the droplet is in equilibrium with the gas phase and I is zero. The evaporation time extends from 5 s at 50% RH to about 25 s at 85% RH.

2.3 Aerosol Hygroscopic Growth from Comparative Kinetic Measurements in the EDB

The mass and heat transport model presented in Section 2.2 is used to compare the evaporation kinetics of probe and sample droplets and to estimate aerosol hygroscopic growth curves from data of the form shown in Figure 1, as follows. The procedure is described below and also outlined in the Supplementary Information. First, the probe droplet evaporation profile is analysed to determine the gas phase RH, which is expressed as a percentage throughout this work; note that a_w is always represented as a fractional value. The probe droplet can be either pure water or a NaCl solution. Davies et al.[32] demonstrated the validity of both methods in the determination of the RH in this kind of comparative kinetic measurements and also estimated the errors on the RH retrieved in both cases.

When a pure water droplet is used as a probe, its experimental radius-squared versus time evaporation profile is compared to simulated evaporation curves at different RH, calculated using equation (5). The mean squared difference (MSD) between the experimental profile and each calculated curve is estimated and the RH corresponding to the curve with the lowest MSD is selected. In this case, the lower and upper values of the RH come from uncertainties in the thermophysical parameters D ($\pm6\%$) and K ($\pm2\%$)[46] in Equation (5) and are given by:

$$RH = RH_w {}^{+(0.169\,RH_w{}^2 - 0.364\,RH_w + 0.194)}_{-(-0.020\,RH_w + 0.021)} \tag{6}$$

When a NaCl solution with known initial concentration is used as a probe, the equilibrated size of the droplet after water evaporation may be used to determine the water activity in the solution, and therefore the RH in the gas phase. In order to do this, the thermodynamic Extended Aerosol Inorganics Model (E-AIM)[5,6,47] (http://www.aim.env.uea.ac.uk/) is used to calculate how water activity and density change with the solution composition during evaporation and to predict the equilibrated radius of the droplet after water evaporation has ended at a given RH. For the relationship between water activity and NaCl concentration, the model is based upon the critical review of Archer,[48] and electrodynamic balance measurements of several authors (see Table 1 of Clegg et al.[49]). Densities of aqueous NaCl (up to and including the hypothetical pure liquid salt) were calculated using the equations of Clegg and Wexler.[39]

The lowest RH value that can be determined with this method is limited by the efflorescence RH of NaCl, which is around 48%. If this equilibrated size method is used, the uncertainties in RH arise from the accuracy with which the equilibrated radius is known (±100 nm) and the uncertainty in the determination of the initial droplet size at $t = 0$ s ($^{+150}_{-100}$ nm), which corresponds to an uncertainty of less than 0.8% of the dry radius for the droplet sizes considered in this work. In this case, the lower and upper values of the RH are expressed as:

$$RH = RH_{eq} {}^{+(-0.0175\,RH_{eq}{}^2 - 0.0005\,RH_{eq} + 0.017)}_{-(-0.0266\,RH_{eq}{}^2 + 0.0086\,RH_{eq} + 0.017)} \tag{7}$$

Using a pure water droplet as a probe of RH is preferable as the equilibrated size method includes a further uncertainty from the initial NaCl solution concentration. Nevertheless, NaCl was used as a probe for measurements at RH < 80% since the associated uncertainties on the RH determined with water as a probe

droplet would be too significant. Uncertainties in the simulation of pure water evaporation become increasingly large below this RH due to uncertainties in the thermophysical parameters D and K and because of the approximation that are needed in the expression of the vapour pressure of water at the droplet surface (discussed further in Section 3.1).

According to Equation (6), the RH can be determined with an uncertainty smaller than $^{+0.33\%}_{-0.3\%}$ for RH values above 90% when pure water is used as a probe. At 50% RH, the error in % RH associated with the determination of RH with the equilibrated size method is $^{+1.2\%}_{-1.5\%}$, according to Equation (7). Knowing the RH with such accuracy is crucial for an accurate application of the kinetics model presented in Section 2.2. The uncertainty of commercial RH probes is typically between ±1% and ±3% in the RH range 10-90% and it usually dramatically increases for RH values above 90%. Both the methods used in this work to retrieve the gas phase RH are associated with smaller uncertainties in the RH determination, especially for measurements at high RH. The RH of the gas phase in the EDB trapping chamber is kept constant during the evaporation measurements, but slight fluctuations in RH can sometimes be observed. However, the RH is monitored frequently with probe droplets during the entire duration of the experiments (5-15 minutes for ten pairs of sample and probe droplets, depending on the RH at which the measurements are taken). The magnitude of these fluctuations is typically smaller or comparable to the uncertainty associated with the RH determination (<0.2-0.3% above 80% RH with water as a probe, <0.5-0.6% below 80% RH with NaCl as a probe).

Once the gas phase RH is known, Equation (5) can be rearranged and solved for a_w in order to calculate the water activity in the droplet at each point in time during evaporation. The particle radius is measured, S_∞ is determined from the probe droplet and the mass flux I can be calculated from the collected radius versus time plot, while all the other quantities are known. For the calculation of mass flux, the radii data must be converted to particle mass values and the density of the droplet is thus needed. The parameterization of density as a function of square-rooted mass fraction of solute has been discussed in Section 2.1. The initial solute *mfs* at t = 0 s is known from the prepared solution and the initial droplet density can be determined. Therefore, considering the measured variation in volume due to the evaporation of water, the *mfs* and density for every measured point during evaporation can be calculated. Knowing how the mass of the droplet varies in time, the mass flux ($I = dm/dt$) can be calculated as the slope of the mass versus time calculated curve and Equation

(5) can be used to determine how the a_w varies in the droplet with time. Over each time-step, the droplet can be considered to be homogeneous in composition; the diffusional mixing time estimated to be 0.01 s for a droplet with a radius of 15 μm and assuming a water diffusion coefficient of $2 \cdot 10^{-9}$ m^2 s^{-1}.

In addition, from the measured radii data and knowing the density of the droplet at each instant, radial growth factor (GF_r) and moles of water per moles of solute (n_{water}/n_{solute}) can be calculated for each measured radii during the evaporation of the sample droplet. Coupling these last quantities with the information about the solution water activity, hygroscopicity curves for the sample compounds can be reported as GF_r vs. a_w, n_{water}/n_{solute} vs. a_w, and mfs vs. a_w. In order to obtain robust hygroscopic data from these comparative kinetics measurements, all curves contain data averaged over at least ten sample droplets. To average the hygroscopicity data calculated from the evaporation of multiple droplets, all the obtained GF_r, n_{water}/n_{solute} and mfs values are separated into a_w bins (0.03-0.005 a_w intervals, depending on the RH at which the measurements are taken) and the data points attributed to each bin are then averaged. The final averaged curves for each compound will be presented in Section 3, unless otherwise specified.

2.4 Materials

Sodium chloride, ammonium sulphate (both ≥99.5%, Sigma-Aldrich) sodium nitrate and sodium sulphate (≥99.5% and ≥99% respectively, Fisher Scientific) solutions were prepared with an initial known mass fraction of solute of ~0.05 for all compounds. In order to make measurements at higher initial a_w values, solutions with an initial known mfs of ~0.005 were also prepared. The gas flow in the EDB chamber was nitrogen (BOC, oxygen-free).

3. RESULTS AND DISCUSSION

3.1 Full Hygroscopicity Curves from Measurements into Different Gas Phase RHs

In deriving hygroscopic growth relationships from droplet evaporation measurements, we must first consider in more detail the accuracy of the framework presented in Section 2.2. The mass transport of water from the droplet to the gas phase during evaporation is coupled to heat transfer, with the latent heat of vaporisation associated with this phase change removed from the droplet. The heat flux from the droplet is greatest when the evaporation rate of water is fastest and, when it is not balanced by the heat flux from the surrounding

11

environment to the droplet, the condensed phase cools down. This temperature depression of the droplet has to be considered because the vapour pressure of water at the surface of the droplet is temperature dependent and directly influences the evaporation rate. In the derivation of Kulmala and co-workers,[42] the dependence of the vapour pressure of the evaporating species at the droplet surface (p_a) on temperature is calculated from the Clausius-Clapeyron equation. The exponential term in this expression is approximated with the first order term in a Taylor series expansion:

$$p_a = a_w p^0(T_{gas}) \exp\left(\frac{LM(T_{droplet} - T_{gas})}{RT_{droplet}T_{gas}}\right)$$

(8)

$$\approx a_w p^0(T_{gas})\left(1 + \frac{LM(T_{droplet} - T_{gas})}{RT_{droplet}T_{gas}}\right)$$

where $p^0(T_{gas})$ is the saturation vapour pressure at the temperature of the gas phase (T_{gas}) and $T_{droplet}$ is the temperature at the droplet surface.

This approximated expression for the temperature dependence of the vapour pressure of water is only accurate when the difference between the droplet and gas phase temperatures is less than ~3°C; beyond this threshold value the approximation with the Taylor series expansion results in an underestimation of the value of the exponential bigger than 1% at 25°C,[42] with a subsequent underestimation of p_a. Consequently, when the droplet temperature depression is large the vapour pressure of water at the surface of the droplet is increasingly underestimated. Therefore, the only measured points that can be used to reliably calculate the water activity in the evaporating sample droplet are those that satisfy this condition. $T_{droplet} - T_{gas}$ can be estimated according to Equation (9):[42]

$$T_{droplet} - T_{gas} = -\frac{IL}{4\pi\beta_T Ka}$$

(9)

Figure 1C shows the time dependence of the calculated $T_{droplet} - T_{gas}$ for the same seven $(NH_4)_2SO_4$ droplets as in the two previous panels. The initial temperature depression can reach -7 K in correspondence to the fastest evaporation rates (at 50% RH), while for the three droplets evaporating into a higher RH (about 78%, 81% and 85%, respectively) the calculated temperature depression is always less than 3 K.

The effect of the droplet temperature depression on the estimated hygroscopic behaviour of a sample compound retrieved from the measurements is shown in Figure 2. Panel A presents the *mfs* versus a_w relationship obtained from a dataset of ten $(NH_4)_2SO_4$ droplets evaporating at 58% RH. A very good agreement with the E-AIM model prediction can be observed for low a_w values, both for the averaged curve and for all the ten single droplets. For higher a_w values, which are derived from the measurements of fluxes at early evaporation times, the water activity calculated with Equation (5) is overestimated and even assumes unrealistic values beyond 1. This arises because the corresponding droplet temperature depression (Figure 2B) is larger in magnitude than the -3 K threshold, which is satisfied only below a calculated a_w of 0.73. The absolute error on the calculation of a_w is shown in Figure 2C. This a_w error was calculated as the difference between the experimental a_w calculated with Equation (5) and the water activity calculated with the E-AIM model at a certain *mfs* value. For the averaged data, the absolute errors on the calculated a_w are very close to 0 at a_w values below 0.73, while they reach values up to about 0.06 when $T_{droplet} - T_{gas}$ is of the order of -5 to -6 K.

As a consequence of this limitation in the kinetics framework, only a portion of about 0.2 in water activity of the *mfs* curve of a sample compound can be retrieved when measurements are taken into an RH at 50%. As a consequence, evaporation measurements into at least three different RHs are need to determine a full curve from 0.5 to >0.99 a_w. An example of this procedure is shown in Figure 3 for the determination of the relationship between a_w and *mfs* for $(NH_4)_2SO_4$, in which EDB results are compared to the E-AIM model prediction (solid black line). Evaporation measurements with a starting solution of ~0.05 *mfs* were made into three different RHs (54%, 74% and 87.3%). A fourth dataset was collected at high RH (90%, more clearly visible in the inset in Figure 3) using a solution with lower starting concentration (*mfs* of 0.005) and therefore with a higher starting a_w (0.997). In this latter case, just a very small section of the *mfs* curve can be calculated: since the droplet had a very low initial concentration, it was not possible to keep it trapped until its a_w equilibrated with the surrounding RH, as it undergoes an exceptionally large size change. The open circles represent data points averaged over ten droplets and have been considered acceptable only if the difference in temperature between the droplet and the gas phase is estimated to be smaller than the 3 K limit. In the background, data for all the ten droplets in the same four datasets are shown. All the data points can be accepted for the two datasets measured at high RH, with the evaporation sufficiently slow to maintain a low droplet

temperature depression, while just small portions of the data measured at 54% and 74% RH can be accepted. The agreement with the a_w vs mfs curve calculated with the E-AIM model is very good for the points that lie within the 3 K threshold for the droplet temperature depression.

One of the interesting features of the comparative kinetics measurements in the cylindrical EDB is that hygroscopic growth curves can be measured up to very high a_w values (>0.99). In Figure 4, the very high end for the measured GF_r, n_{water}/n_{solute} and mfs versus water activity plots are shown for $(NH_4)_2SO_4$, and are compared with simulations from the E-AIM model (grey solid lines). In this case, the highest a_w reached with this averaged dataset is 0.997, corresponding to a GF_r value of 6.22 (Figure 4A). For the calculation of the radial growth curve, the dry radius of the droplets is calculated from the wet size at $t = 0$ s, the concentration of the starting solution and the density of crystalline ammonium sulphate (1.77 g cm^{-3})[41]. In Figure 4B, at a_w = 0.997 the number of absorbed moles of water per moles of $(NH_4)_2SO_4$ inferred from the measurements is close to 1000 and the agreement between the measured value and the E-AIM model prediction is remarkable. If the mfs vs. a_w plot is considered (Figure 4C), the lowest measured ammonium sulphate mass fraction is 0.005 at a_w = 0.997. It is also worth noting that not only is it possible to measure growth curves up to very high water activity values with this technique, but also that the accuracy on the calculated a_w is highest when the RH at which measurements are taken is high (>90%), according to Equations (6) and (7). It should also be stressed that the growth curve is retrieved in a matter of seconds, potentially allowing accurate hygroscopic growth measurements for droplets containing volatile components, provided their vapour pressure is less than that of water

3.2 Accuracy of Measurements

Hygroscopicity measurements on four well-characterized inorganic-aqueous systems (NaCl, Na$_2$SO$_4$, NaNO$_3$ and $(NH_4)_2SO_4$) were performed in order to confirm the validity of the method over the range in a_w from 0.5 to 0.99. The relationships between mfs and a_w for each solute are shown in Figure 5, compared with the corresponding prediction from the E-AIM model. The level of agreement obtained is excellent for all the systems studied. Na$_2$SO$_4$ was observed to crystallize during measurements at a_w = 0.57 and therefore it was not possible to reach lower water activity values during the experiments. In addition, the systematic over-predictions of E-AIM between water activities of 0.75 and 0.85 and under-predictions at the lowest a_w are

14

consistent with previous observations (see, for example, Figure 3 of Clegg et al.[49]). It should be noted that the measurement for aqueous sodium chloride droplet provides a consistency check of the approach for inferring the hygroscopicity from kinetics measurements. For control sodium chloride droplets, measurements of the final equilibrated size are used to infer the RH of the gas flow. This value is then used in the retrieval of the *mfs* data from the kinetic measurement at all intermediate non-equilibrated a_w values; in combination, this allows confirmation of the shape of the *mfs* vs a_w dependence at all intermediate water activities.

Osmotic coefficients, ϕ, provide a convenient way to characterise the departure of solutes from ideality and can be determined from the equation:

$$\phi = -\frac{\ln(a_w)}{M_w m_i v_i} \qquad (10)$$

where M_w is the molecular weight of water, m_i is the molality of the solute i and v_i is the stoichiometric coefficient of solute i. As the water activity tends to unity at zero solute molality, the osmotic coefficient should tend to 1 with the expected Debye-Hückel limiting law behaviour. In Figure 6 we report the dependence of the osmotic coefficient on solute molality for the four binary systems studied, providing a stringent examination of the retrieved hygroscopic behaviour particularly at the dilute solution limit. As expected, the dependence of the osmotic coefficient on water activity leads to large uncertainties at low molality, a consequence of the large uncertainties in water activity in the early stages of evaporation (high mass flux) of dilute solution droplets. At molalities higher than 1 mol kg^{-1}, the close agreement between the measured and modelled osmotic coefficients for all systems suggests that the uncertainties attributed to measurements at these molalities are conservative. Deviations are typically <0.02 in osmotic coefficient for the $(NH_4)_2SO_4$, $NaNO_3$ and $NaCl$ systems, comparable to previous measurements (see for example, the comparisons of predictions and measurements of osmotic coefficients in the work by Clegg et al.[47]). Larger discrepancies are observed for Na_2SO_4 at intermediate concentrations and these have already been discussed above.

To better illustrate the agreement between the experimental results and simulations from the E-AIM model, Figure 7 provides a comparison between the measured and modelled n_{water}/n_{solute} ratios for the four inorganic systems, spanning the range from just 3 water molecules per ion pair up to 1000. For each point in the plot, n_{water}/n_{solute} was calculated with the E-AIM model at the exact a_w value of the experimental data point. For

15

n_{water}/n_{solute} values up to about 100 (corresponding to a_w of up to about 0.98, depending on the salt), all the points lie close to the 1:1 line, thus revealing a very good agreement of the experimental results with the E-AIM model calculations. For $n_{water}/n_{solute} > 100$, the points appear a little more scattered. This is due to the fact that at very high a_w values, even a slight variation in water activity results in a significant variation in the calculated water moles values, with the hygroscopic growth curve extremely steep in this region. As an example, the highest measured data point for $(NH_4)_2SO_4$ can be considered: the measured a_w is 0.997 and it corresponds to 799 n_{water}/n_{solute} calculated with the E-AIM model; if an uncertainty of ±0.001 in a_w is considered, the calculated n_{water}/n_{solute} values are 585 and 1236 for water activity values of 0.996 and 0.998, respectively. In order to show the effect of such a small uncertainty on water activity, in Figure 7 the uncertainty on the calculated n_{water}/n_{solute} for ammonium sulphate is represented with dark and light grey envelopes if an error of ±0.001 and ±0.002 in a_w is considered, respectively. These envelopes become increasingly large when the amount of absorbed water increases because of the steepness of the hygroscopic growth curve in that region.

3.3 Sensitivity to Small Changes in Chemical Composition

Hygroscopic growth measurements on mixtures of NaCl and $(NH_4)_2SO_4$ were also taken in order to evaluate the sensitivity of the experimental method to small changes in the chemical composition of the aerosol droplets. Three different $(NH_4)_2SO_4$/NaCl mass ratios were considered (50/50, 90/10 and 95/5) and the *mfs* and *GF$_r$* vs. a_w experimental curves (circles) are compared with simulations from the E-AIM model (dashed lines) in Figure 8. For the calculation of growth factors of these mixtures, the reference dry state is considered to be a solid particle made of non-mixed crystalline ammonium sulphate and sodium chloride. The dry density is calculated estimating the dry volumes separately for NaCl and $(NH_4)_2SO_4$ and calculating the ratio between the total mass and the total volume of the two dry salts.

The experimental results show an overall good agreement with the curves predicted by the E-AIM model for all three mixtures considered, both for the *mfs* and for the *GF$_r$* curves. The obtained *mfs* vs. a_w plot (Figure 8A) shows that it is possible to successfully characterise the different hygroscopic behaviours of the 90/10 and 95/5 mixtures up to about $a_w = 0.93$. Above this value, the trends for the 90/10 and 95/5 mixtures become very similar: the difference between the two curves is less than 0.01 *mfs* and discriminating between them is not

16

possible. When the experimental results are plotted as GF_r vs. a_w (Figure 8B), the predicted curves for the same two mass ratios differ by 0.021 in GF_r at $a_w = 0.65$ and by 0.058 in GF_r at $a_w = 0.95$; in this range, it was possible to discriminate between their GF_r trends with the EDB measurements. For higher water activity values, the hygroscopic growth curve becomes steep and differences between the two trends are not discernible. The comparison could not be carried out for the ratio n_{water}/n_{solute} because the curves predicted by the E-AIM model for the 90/10 and 95/5 mixtures are both essentially indistinguishable from that of ammonium sulphate.

These results show that it is possible with this technique to detect variations in the hygroscopicity of solutions with only slight differences in chemical compositions, down to a 5% difference on a mass basis for mixtures of NaCl and $(NH_4)_2SO_4$. In the case of different mixtures, the minimum detectable variation would depend on the nature of their components: greater discrimination would be achieved if the individual pure components were to much more dissimilar hygroscopic properties.

3.4 Sensitivity to the Value of the Mass Accommodation Coefficient

The sensitivity of these hygroscopicity measurements to variations in the mass accommodation coefficient (α_M) was also investigated. The mass accommodation coefficient represents the fraction of water molecules that is absorbed in to the droplet bulk on collision with the surface, considered equivalent to the evaporation coefficient by the principle of microscopic reversibility. In the literature, measurements of the mass accommodation coefficient have been performed with a number of different techniques and resulting in a considerable range of different α_M values.[46,50,51] α_M contributes to the mass transition correction factor (β_M, Equation 5) in the kinetics model used here. Up to this point we have assumed that α_M has a value equal to 1, in agreement with previous studies which have reported the value of α_M for water accommodating/evaporation from a water surface.[23,46,52] Similar to α_M, the thermal accommodation coefficient (α_T) indicates the efficiency with which a colliding water molecule is able to transfer energy to the droplet and is included in the expression for β_T, the heat transition correction factor. For all the results presented in the previous Sections and for the analysis discussed here, α_T was maintained constant at 1, in agreement with literature studies on aqueous solution droplets,[51,53] and the possible effects of its variation have not been investigated.

In previous work,[34] we have examined the influence of the uncertainty in α_M on the evaporation kinetics profiles of aqueous solutions. We have shown that the evaporation kinetics measurements for droplets with radii larger than 5 μm are insensitive to variations in α_M when >0.05 when the uncertainties resulting from the remaining thermophysical parameters and the experimental conditions are considered. Here the influence of α_M on the obtained hygroscopic growth curve of NaCl expressed in terms of n_{water}/n_{solute} for NaCl is considered over the entire range of RH investigated in this work (from 50% to above 99% RH). In Figure 9, the black circles represent the original growth curve calculated with $\alpha_M = 1$, while the grey open circles represent the n_{water}/n_{solute} for the same evaporating droplets datasets but with the analysis performed assuming $\alpha_M = 0.1$. A slight shift in the water activity calculated with Equation 5 can be observed when varying the value of the mass accommodation coefficient, especially for a_w values above 0.95 where the growth curve becomes very steep. Nevertheless, the two curves can be considered to be very similar within the experimental errors. The superior agreement of the curve calculated with $\alpha_M = 1$ (black circles) and the prediction from the E-AIM model (black solid line) at very high a_w, together with the very good results obtained for all the aerosol systems presented in Sections 3.2 and 3.3, suggests that assuming a value of $\alpha_M = 1$ most accurately characterises the mass transport behaviour observed in the evaporating droplets for all of the binary and ternary systems studied here.

4. CONCLUSIONS

Using the comparative kinetics technique, we have shown that equilibrium hygroscopic growth measurements can be made with typical accuracies in water activity of better than <±0.2 % at water activities >0.9 (see, for example, Figure 7) and ~±1 % below 80 % RH. Conventional instruments report growth under sub-saturated conditions with accuracies of ±1% in a_w below 95% RH and ±0.1% for high humidity instruments at >99% RH.[14,16,30] In CCN activation measurements, the uncertainty in the critical supersaturation value is typically between 30% at supersaturations between 0.1-1%, equivalent to uncertainties of 0.03 to 0.3 % at a_w >0.99.[31] In addition, the largest uncertainties in diameter growth factor from this technique are of order ~0.7 % (see, for example, the points that have error bars larger than the point size in Figure 8); sub-saturated growth measurements by conventional instruments have associated uncertainties of ±5 % with large inter-instrument variabilities.[16,26] Indeed, the hygroscopic growth curves for mixed component aerosol containing $(NH_4)_2SO_4$ / NaCl mass ratios of 90/10 and 95/5 shown in Figure 8 are clearly resolved: the difference between

growth factors for these two systems varies from 0.02 at 65 % RH (at growth factors of ~1.34, *i.e.* a 1.5 % difference) up to 0.07 at 98 % RH (at growth factors of ~3.20, *i.e.* a 2 % difference). Such a small effect would unlikely be resolved in conventional instruments.

The instrument described here has some significant benefits for rapidly surveying the hygroscopic growth of laboratory generated aerosols of known composition or, indeed, samples from field measurements. Determinations of hygroscopic growth can be made over a wide range in water activity by measuring the time-dependent profiles of droplets evaporating into a selected sequence of RHs (potentially down to fully dry conditions and up to water activities greater than 0.99) with a similar level of accuracy and without particular refinement to address specific water activity ranges. The opportunity to measure hygroscopic growth to such high water activity should provide an opportunity to address some of the challenges in resolving the discrepancies between determinations of κ from measurements made under sub-saturated and super-saturated conditions. An advantage of performing measurements on coarse mode particles (>5 μm in diameter) is that the Kelvin component of the equilibrium response is negligible when compared with the solute component. Thus, the surface curvature component can be ignored, providing the most unambiguous route to accurate measurements of the solute effect. In addition, this approach yields growth curves in a few seconds starting from the limit of high water activity, particularly valuable for studying organic compounds of low-solubility or high volatility by avoiding the complications that follow when changes in the particle-gas partitioning of the VOC/SVOC must be considered. Hygroscopic growth measurements can also be made over a wide temperature range from <250 to >320 K although we focus on ambient temperatures in this publication. Although not appropriate for direct field measurements on accumulation mode particles, the technique can be used to characterise samples with volumes of only a few 10's of microliters, the minimum volume required to load the piezoelectric droplet-on-demand generators used to deliver droplets to the electrodynamic balance. Benefiting from these advantages, present measurements are underway to provide accurate measurements of hygroscopic growth for a wide range of organic components found in ambient aerosol containing disparate functional groups and containing multiple functionalities in the same solute molecule.

SUPPORTING INFORMATION

Further details of the procedure for the retrieval of hygroscopic growth curves from evaporation profiles are available free of charge via the Internet at http://pubs.acs.org. The experimental data presented in the Figures are provided through the University of Bristol data repository at Reid, J. P. (2015): DOI: 10.5523/bris.h8igni7g424s19a8ab3boyjb5.

REFERENCES

(1)   Dusek, U.; Frank, G. P.; Hildebrandt, L.; Curtius, J.; Schneider, J.; Walter, S.; Chand, D.; Drewnick, F.; Hings, S.; Jung, D.; et al. Size Matters More than Chemistry for Cloud-Nucleating Ability of Aerosol Particles. *Science* **2006**, *312* (5778), 1375–1378.

(2)   Topping, D.; Connolly, P.; McFiggans, G. Cloud Droplet Number Enhanced by Co-Condensation of Organic Vapours. *Nat. Geosci.* **2013**, *6*, 443–446.

(3)   Haddrell, A. E.; Davies, J. F.; Reid, J. P. Dynamics of Particle Size on Inhalation of Environmental Aerosol and Impact on Deposition Fraction. *Environ. Sci. Technol.* **2015**, *49* (24), 14512–14521.

(4)   Ervens, B. Influence of Water-Soluble Organic Carbon on Cloud Drop Number Concentration. *J. Geophys. Res.* **2005**, *110* (D18), D18211.

(5)   Clegg, S. L.; Brimblecombe, P.; Wexler, A. S. Thermodynamic Model of the System H^+-NH_4^+-SO_4^{2-}-NO_3^--H_2O at Tropospheric Temperatures. *J. Geophys. Res.* **1998**, *102* (12), 2137–2154.

(6)   Wexler, A. S.; Clegg, S. L. Atmospheric Aerosol Models for Systems Including the Ions H^+, NH_4^+, Na^+, SO_4^{2-}, NO_3^-, Cl^-, Br^-, and H_2O. *J. Geophys. Res. Atmos.* **2002**, *107* (D14), 4207.

(7)   Topping, D. O.; McFiggans, G. B.; Coe, H. A Curved Multi-Component Aerosol Hygroscopicity Model Framework: Part 2 - Including Organics Compounds. *Atmos. Chem. Phys.* **2005**, *5*, 1223 - 1242.

(8)   Topping, D. O.; Mcfiggans, G. B.; Coe, H. And Physics A Curved Multi-Component Aerosol Hygroscopicity Model Framework : Part 1 – Inorganic Compounds. *Atmos. Chem. Phys.* **2005**, *5*, 1205–1222.

(9)   Zuend, A.; Marcolli, C.; Booth, A. M.; Lienhard, D. M.; Soonsin, V.; Krieger, U. K.; Topping, D. O.; McFiggans, G.; Peter, T.; Seinfeld, J. H. New and Extended Parameterization of the Thermodynamic Model AIOMFAC: Calculation of Activity Coefficients for Organic-Inorganic Mixtures Containing Carboxyl, Hydroxyl, Carbonyl, Ether, Ester, Alkenyl, Alkyl, and Aromatic Functional Groups. *Atmos. Chem. Phys.* **2011**, *11* (17), 9155–9206.

(10)   Zuend, A.; Marcolli, C.; Luo, B. P.; Peter, T. A Thermodynamic Model of Mixed Organic-Inorganic Aerosols to Predict Activity Coefficients. *Atmos. Chem. Phys.* **2008**, *8*, 4559-4593.

(11)   Kreidenweis, S. M.; Petters, M. D.; DeMott, P. J. Single-Parameter Estimates of Aerosol Water Content. *Environ. Res. Lett.* **2008**, *3*, 035002.

(12)   Petters, M. D.; Kreidenweis, S. M. A Single Parameter Representation of Hygroscopic Growth and Cloud Condensation Nucleus Activity. *Atmos. Chem. Phys.* **2007**, *7*, 1961–1971.

(13)   Chang, R. Y.-W.; Slowik, J. G.; Shantz, N. C.; Vlasenko, A.; Liggio, J.; Sjostedt, S. J.; Leaitch, W. R.; Abbatt, J. P. D. The Hygroscopicity Parameter (κ) of Ambient Organic Aerosol at a Field Site Subject to Biogenic and Anthropogenic Influences: Relationship to Degree of Aerosol Oxidation. *Atmos. Chem. Phys.* **2010**, *10* (11), 5047–5064.

(14)   Duplissy, J.; DeCarlo, P. F.; Dommen, J.; Alfarra, M. R.; Metzger, A.; Barmpadimos, I.; Prevot, A. S. H.; Weingartner, E.; Tritscher, T.; Gysel, M.; et al. Relating Hygroscopicity and Composition of Organic Aerosol Particulate Matter. *Atmos. Chem. Phys.* **2011**, *11*, 1155–1165.

(15)   Rickards, A. M. J.; Miles, R. E. H.; Davies, J. F.; Marshall, F. H.; Reid, J. P. Measurements of the Sensitivity of Aerosol Hygroscopicity and the κ Parameter to the O/C Ratio. *J. Phys. Chem. A* **2013**, *117* (51), 14120–14131.

(16)   Good, N.; Topping, D. O.; Duplissy, J.; Gysel, M.; Meyer, N. K.; Metzger, a.; Turner, S. F.;

Baltensperger, U.; Ristovski, Z.; Weingartner, E.; et al. Widening the Gap between Measurement and Modelling of Secondary Organic Aerosol Properties? *Atmos. Chem. Phys.* **2010**, *10*, 2577–2593.

(17)   Petters, M. D.; Kreidenweis, S. M. A Single Parameter Representation of Hygroscopic Growth and Cloud Condensation Nucleus Activity - Part 3: Including Surfactant Partitioning. *Atmos. Chem. Phys.* **2013**, *13* (2), 1081–1091.

(18)   Pajunoja, A.; Lambe, A. T.; Hakala, J.; Rastak, N.; Cummings, M. J.; Brogan, J. F.; Hao, L.; Paramonov, M.; Hong, J.; Prisle, N. L.; et al. Adsorptive Uptake of Water by Semisolid Secondary Organic Aerosols In the Atmosphere. *Nat. Geosci.* **2014**, 3063–3068.

(19)   You, Y.; Smith, M. L.; Song, M.; Martin, S. T.; Bertram, A. K. Liquid–liquid Phase Separation in Atmospherically Relevant Particles Consisting of Organic Species and Inorganic Salts. *Int. Rev. Phys. Chem.* **2014**, 33, 43-77.

(20)   Topping, D.; Barley, M.; McFiggans, G. Including Phase Separation in a Unified Model to Calculate Partitioning of Vapours to Mixed Inorganic–organic Aerosol Particles. *Faraday Discuss.* **2013**, *165*, 273.

(21)   Sareen, N.; Schwier, A. N.; Lathem, T. L.; Nenes, A.; McNeill, V. F. Surfactants from the Gas Phase May Promote Cloud Droplet Formation. *Proc. Natl. Acad. Sci. U.S.A.* **2013**, *110* (8), 2723–2728.

(22)   Nozière, B.; Baduel, C.; Jaffrezo, J.-L. The Dynamic Surface Tension of Atmospheric Aerosol Surfactants Reveals New Aspects of Cloud Activation. *Nat. Commun.* **2014**, *5*, 1–7.

(23)   Davies, J. F.; Miles, R. E. H.; Haddrell, A. E.; Reid, J. P. Temperature Dependence of the Vapor Pressure and Evaporation Coefficient of Supercooled Water. *J. Geophys. Res. Atmos.* **2014**, *119* (18), 10931–10940.

(24)   Vehkamäki, H.; Riipinen, I. Thermodynamics and Kinetics of Atmospheric Aerosol Particle Formation and Growth. *Chem. Soc. Rev.* **2012**, *41*, 5160.

(25)   Kolb, C. E.; Cox, R. A.; Abbatt, J. P. D.; Ammann, M.; Davis, E. J.; Donaldson, D. J.; Garrett, B. C.;

George, C.; Griffiths, P. T.; Hanson, D. R.; et al. An Overview of Current Issues in the Uptake of Atmospheric Trace Gases by Aerosols and Clouds. *Atmos. Chem. Phys.* **2010**, *10* (21), 10561–10605.

(26) Suda, S. R.; Petters, M. D. Accurate Determination of Aerosol Activity Coefficients at Relative Humidities up to 99% Using the Hygroscopicity Tandem Differential Mobility Analyzer Technique. *Aerosol Sci. Technol.* **2013**, *47* (9), 991–1000.

(27) Krieger, U. K.; Marcolli, C.; Reid, J. P. Exploring the Complexity of Aerosol Particle Properties and Processes Using Single Particle Techniques. *Chem. Soc. Rev.* **2012**, *41* (19), 6631.

(28) Wex, H.; Petters, M. D.; Carrico, C. M.; Hallbauer, E.; Massling, A.; McMeeking, G. R.; Poulain, L.; Wu, Z.; Kreidenweis, S. M.; Stratmann, F. Towards Closing the Gap between Hygroscopic Growth and Activation for Secondary Organic Aerosol: Part 1 – Evidence from Measurements. *Atmos. Chem. Phys.* **2009**, *9*, 3987–3997.

(29) Walker, J. S.; Wills, J. B.; Reid, J. P.; Wang, L.; Topping, D. O.; Butler, J. R.; Zhang, Y.-H. Direct Comparison of the Hygroscopic Properties of Ammonium Sulfate and Sodium Chloride Aerosol at Relative Humidities Approaching Saturation. *J. Phys. Chem. A* **2010**, *114* (48), 12682–12691.

(30) McFiggans, G.; Artaxo, P.; Baltensperger, U.; Coe, H.; Facchini, M. C.; Feingold, G.; Fuzzi, S.; Gysel, M.; Laaksonen, A.; Lohmann, U.; et al. The Effect of Physical and Chemical Aerosol Properties on Warm Cloud Droplet Activation. *Atmos. Chem. Phys.* **2006**, *6*, 2593-2649.

(31) Rose, D.; Frank, G. P.; Dusek, U.; Gunthe, S. S.; Andreae, M. O.; Pöschl, U. Calibration and Measurement Uncertainties of a Continuous-Flow Cloud Condensation Nuclei Counter (DMT-CCNC): CCN Activation of Ammonium Sulfate and Sodium Chloride Aerosol Particles in Theory and Experiment. *Atmos. Chem. Phys.* **2008**, *8*, 1153-1179.

(32) Davies, J. F.; Haddrell, A. E.; Rickards, A. M. J.; Reid, J. P. Simultaneous Analysis of the Equilibrium Hygroscopicity and Water Transport Kinetics of Liquid Aerosol. *Anal. Chem.* **2013**, *85* (12), 5819–5826.

(33) Davies, J. F.; Haddrell, A. E.; Reid, J. P. Time-Resolved Measurements of the Evaporation of Volatile

Components from Single Aerosol Droplets. *Aerosol Sci. Technol.* **2012**, *46* (6), 666–677.

(34)   Davies, J. F.; Haddrell, A. E.; Miles, R. E. H.; Bull, C. R.; Reid, J. P. Bulk, Surface, and Gas-Phase Limited Water Transport in Aerosol. *J. Phys. Chem. A* **2012**, *116* (45), 10987–10998.

(35)   Heinisch, C.; Wills, J. B.; Reid, J. P.; Tschudi, T.; Tropea, C. Temperature Measurement of Single Evaporating Water Droplets in a Nitrogen Flow Using Spontaneous Raman Scattering. *Phys. Chem. Chem. Phys.* **2009**, *11* (42), 9720–9728.

(36)   Glantschnig, W. J.; Chen, S. H. Light Scattering from Water Droplets in the Geometrical Optics Approximation. *Appl. Opt.* **1981**, *20* (14), 2499–2509.

(37)   Liu, Y.; Daum, P. H. Relationship of Refractive Index to Mass Density and Self-Consistency of Mixing Rules for Multicomponent Mixtures like Ambient Aerosols. *J. Aerosol Sci.* **2008**, *39* (11), 974–986.

(38)   Cotterell, M.; Mason, B. J.; Preston, T. C.; Orr-Ewing, A.; Reid, J. P. Optical Extinction Efficiency Measurements on Fine and Accumulation Mode Aerosol Using Single Particle Cavity Ring-Down Spectroscopy. *Phys. Chem. Chem. Phys.* **2015**, *17*, 15843–15856.

(39)   Clegg, S. L.; Wexler, A. S. Densities and Apparent Molar Volumes of Atmospherically Important Electrolyte Solutions. 1. The Solutes H_2SO_4, HNO_3, HCl, Na_2SO_4, $NaNO_3$, NaCl, $(NH_4)_2SO_4$, NH_4NO_3 and NH_4Cl from 0 to 50 °C, Including Extrapolations to Very Low Temperature and to the Pure Liquid State, and $NaHSO_4$, NaOH, and NH_3 at 25 °C. *J. Phys. Chem. A* **2011**, *115* (15), 3393-3460.

(40)   Janz, G. J. Thermodynamc and Transport Properties of Molten Salts: Correlation Equations for Critically Evaluated Density, Surface Tension, Electrical Conductance, and Viscosity Data. *J. Phys. Chem. Ref. Data* **1988**, *17,* Supplement 2, 309 pages.

(41)   Lide, D. R. *CRC Handbook of Chemistry and Physics, 85th Ed.*; CRC Press, 2005.

(42)   Kulmala, M.; Vesala, T.; Wagner, P. E. An Analytical Expression For the Rate of Binary Condensational Particle Growth. *Proc. R. Soc. A Math. Phys. Eng. Sci.* **1993**, *441* (1913), 589–605.

(43)   Hopkins, R. J.; Reid, J. P. Evaporation of Ethanol/water Droplets: Examining the Temporal Evolution

of Droplet Size, Composition and Temperature. *J. Phys. Chem. A* **2005**, *109* (35), 7923–7931.

(44)   Nielsen, J. K.; Maus, C.; Rzesanke, D.; Leisner, T. Charge Induced Stability of Water Droplets in Subsaturated Environment. *Atmos. Chem. Phys.* **2011**, *11* (5), 2031–2037.

(45)   Miles, R. E. H.; Knox, K. J.; Reid, J. P.; Laurain, A. M. C.; Mitchem, L. Measurements of Mass and Heat Transfer at a Liquid Water Surface during Condensation or Evaporation of a Subnanometer Thickness Layer of Water. *Phys. Rev. Lett.* **2010**, *105* (11), 1–4.

(46)   Miles, R. E. H.; Reid, J. P.; Riipinen, I. Comparison of Approaches for Measuring the Mass Accommodation Coefficient for the Condensation of Water and Sensitivities to Uncertainties in Thermophysical Properties. *J. Phys. Chem. A* **2012**, *116* (44), 10810–10825.

(47)   Clegg, S. L.; Brimblecombe, P.; Wexler, A. S. Thermodynamic Model of the System $H^+-NH_4^+-Na^+-SO_4^{2-}-NO_3^--Cl^--H_2O$ at 298.15 K. *J. Phys. Chem. A* **1998**, *102* (12), 2155–2171.

(48)   Archer, D. G. Thermodynamic Properties of the $NaCl+H_2O$ System. II. Thermodynamic Properties of $NaCl_{(aq)}$, $NaCl.2H_2O_{(cr)}$, and Phase Equilibria. *J. Phys. Chem. Ref. Data* **1992**, *21* (4), 793.

(49)   Clegg, S. L.; Brimblecombe, P.; Liang, Z.; Chan, C. K. Thermodynamic Properties of Aqueous Aerosols to High Supersaturation: II—A Model of the System $Na^+-Cl^--NO_3^--SO_4^{2-}-H_2O$ at 298.15 K. *Aerosol Sci. Technol.* **1997**, *27* (3), 345–366.

(50)   Davidovits, P.; Kolb, C. E.; Williams, L. R.; Jayne, J. T.; Worsnop, D. R. Mass Accommodation and Chemical Reactions at Gas-Liquid Interfaces. *Chem. Rev.* **2006**, *106*, 1323–1354.

(51)   Winkler, P. M.; Vrtala, A.; Rudolf, R.; Wagner, P. E.; Riipinen, I.; Vesala, T.; Lehtinen, K. E. J.; Viisanen, Y.; Kulmala, M. Condensation of Water Vapor: Experimental Determination of Mass and Thermal Accommodation Coefficients. *J. Geophys. Res.* **2006**, *111* (D19), D19202.

(52)   Julin, J.; Shiraiwa, M.; Miles, R. E. H.; Reid, J. P.; Pöschl, U.; Riipinen, I. Mass Accommodation of Water: Bridging the Gap between Molecular Dynamics Simulations and Kinetic Condensation Models. *J. Phys. Chem. A* **2013**, *117* (2), 410–420.

(53)   Li, Y. Q.; Davidovits, P.; Kolb, C. E.; Worsnop, D. R. Mass and Thermal Accommodation Coefficients of H_2O(g) on Liquid Water as a Function of Temperature. *J. Phys. Chem. A* **2001**, *105* (47), 10627–10634.

Figure 1. (A) Measured radii (μm) of seven $(NH_4)_2SO_4$ solution droplets (initial *mfs* of about 0.05) evaporating into different RHs at 20°C. Red to blue curves indicate increasing RH in the gas phase at approximately equally spaced intervals in RH, from ~50% (red) to ~85% (blue) RH. The method for determining the RH exactly is described in Section 2.3. (B) For the same droplets, the calculated mass flux (ng s^{-1}) from the droplet is plotted against time. (C) Variation in time of the difference between the temperature (K) of the droplet surface ($T_{droplet}$) and the gas phase (T_{gas}), calculated according to Equation (9).
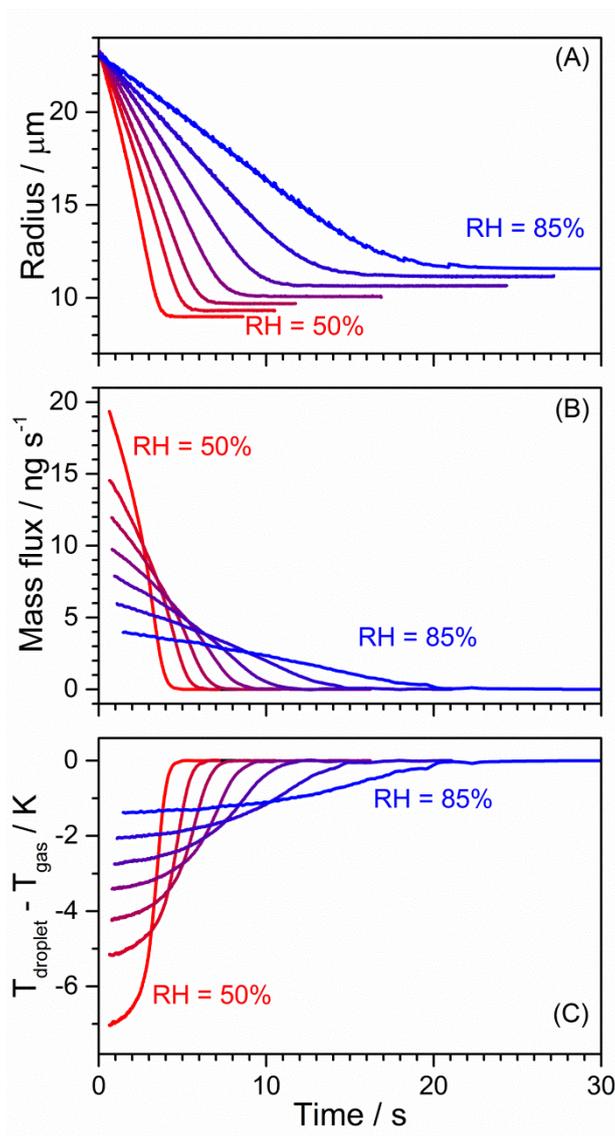
Figure 2. (A) Mass fraction of solute (*mfs*) vs. a_w plot, calculated from the evaporation kinetics of 10 $(NH_4)_2SO_4$ droplets evaporating in to 58% RH. Symbols: grey dots – data from each individual droplet; black dots – averaged curve calculated over the 10 droplet dataset; solid line – *mfs* vs. a_w for $(NH_4)_2SO_4$ calculated with the E-AIM model. (B) Difference in temperature between the droplet surface and the surrounding gas phase as a function of a_w, calculated with Equation (9). (C) Absolute error in a_w relative to the reference E-AIM model values. Symbols: grey squares – error on a_w from each individual droplet; open black squares - error on a_w relative to the averaged *mfs* curve.
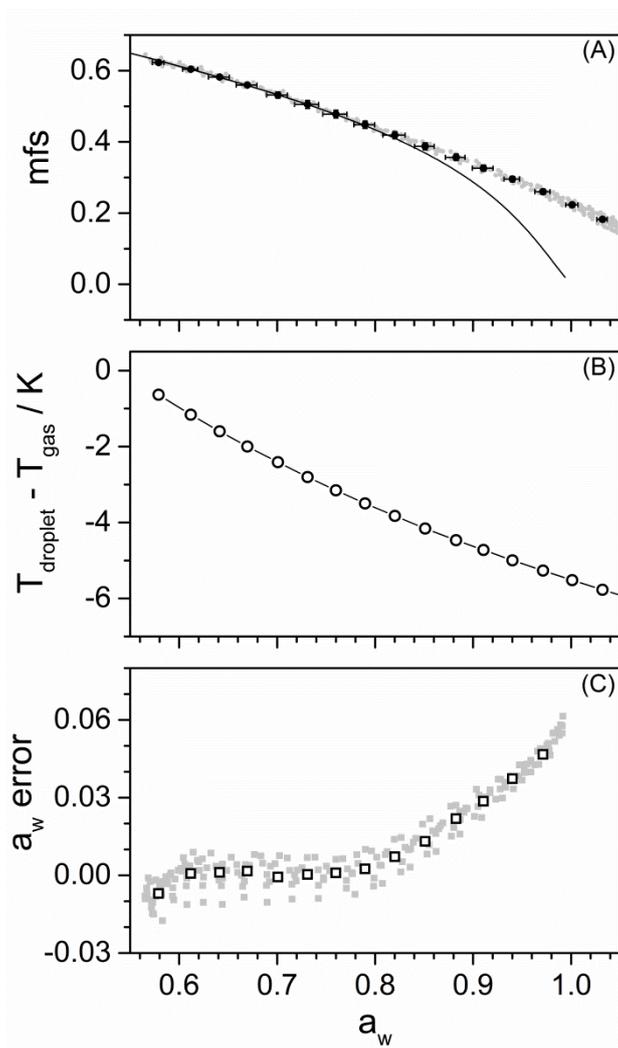
Figure 3. Retrieval of the full *mfs* vs. a_w curve of ammonium sulphate from measurements into different RHs. Symbols: solid line – calculated *mfs* vs. a_w curve from the E-AIM model; filled circles – individual data from all 10 droplets in each data set; open circles – averaged data for which the maximum 3 K droplet temperature depression condition is satisfied. Colours: red, purple and light blue – droplets of 0.05 *mfs* starting solution evaporating into a gas phase at 54%, 74% and 87.3% RH, respectively; dark blue – 0.005 *mfs* starting solution into a gas phase 90% RH. Note: error bars are smaller than the data point when not shown.
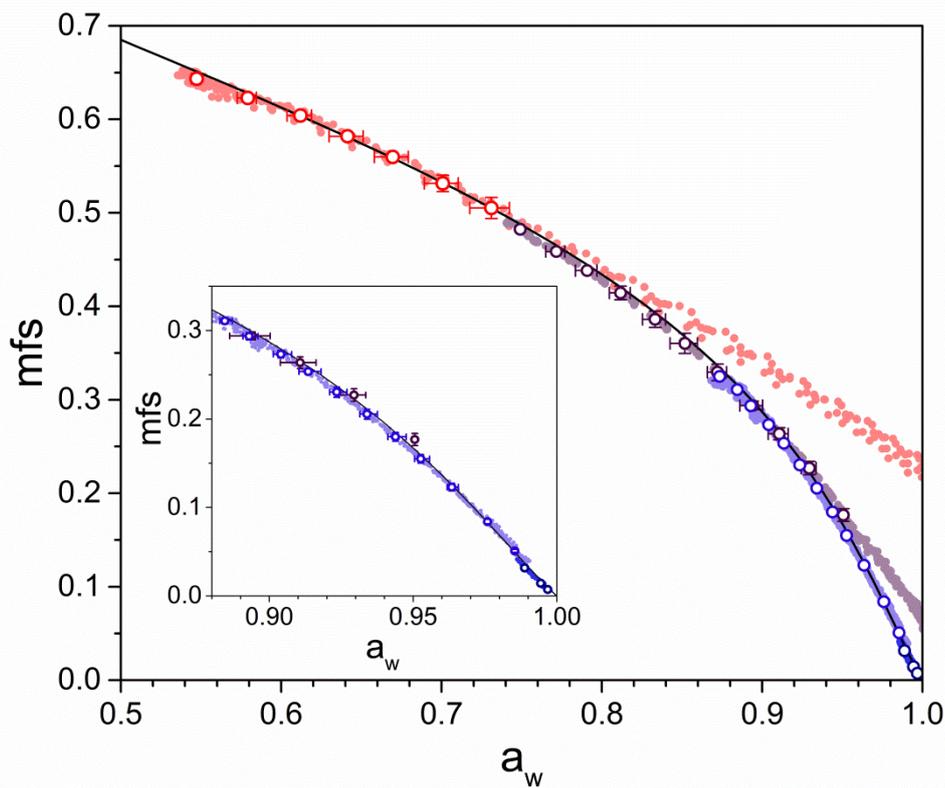
Figure 4. GF_r, n_{water}/n_{solute} and *mfs* for a_w values between 0.88 and 1 for $(NH_4)_2SO_4$. Symbols: filled circles – experimental data points averaged over a minimum of 10 droplets; solid lines – calculated curves from the E-AIM model. Note: error bars are smaller than the data point when not shown.
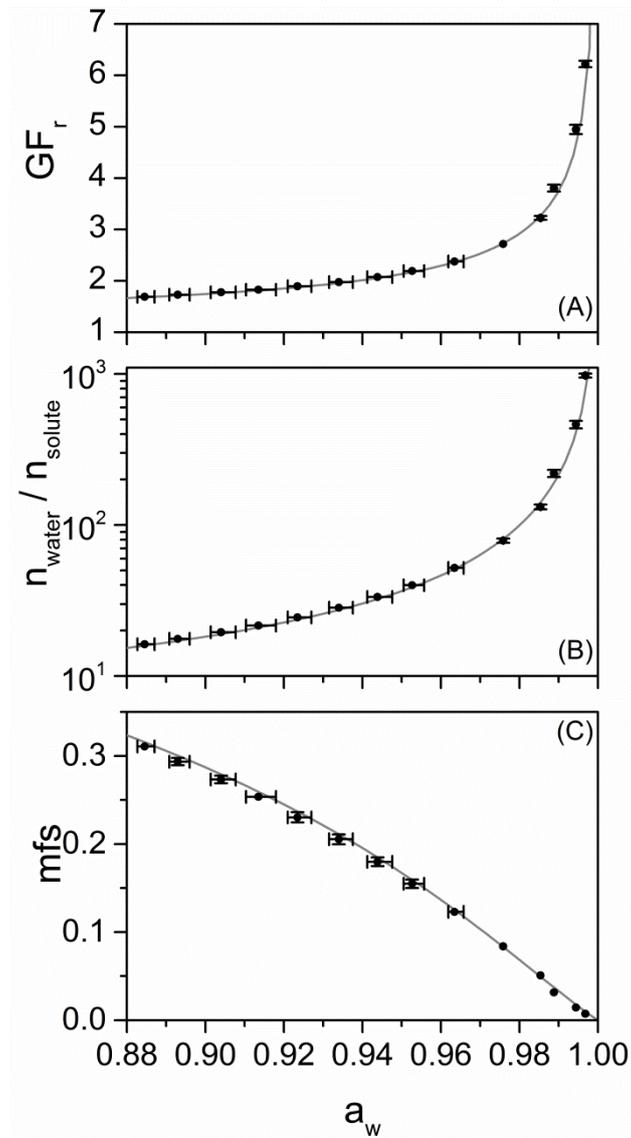
Figure 5. Measured *mfs* vs. a_w plots for $(NH_4)_2SO_4$, $NaNO_3$, Na_2SO_4 and NaCl (panels A-D). Symbols: filled circles – experimental data; solid lines – calculation from the E-AIM model. Note: error bars are smaller than the data point when not shown.
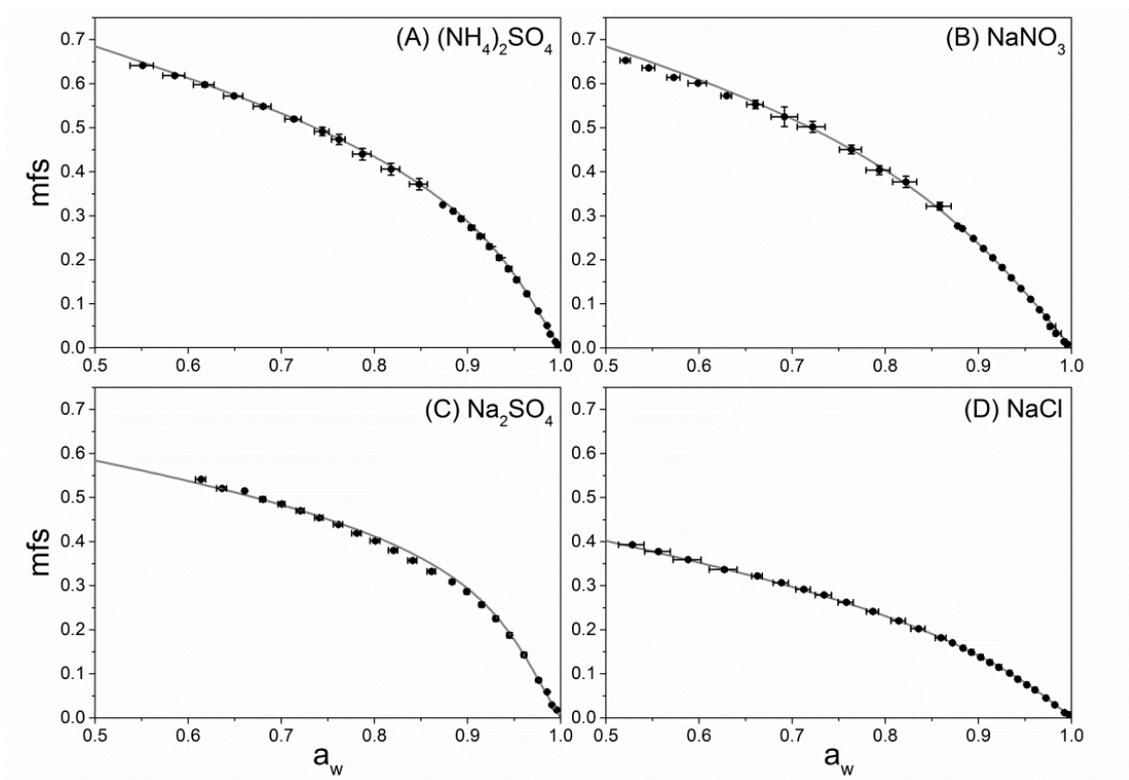
Figure 6. Dependence of osmotic coefficient on molality of solute (mol kg^{-1}) for $(NH_4)_2SO_4$, $NaNO_3$, Na_2SO_4 and NaCl (panels A-D). Symbols: filled circles – experimental data; solid lines – calculation from the E-AIM model.
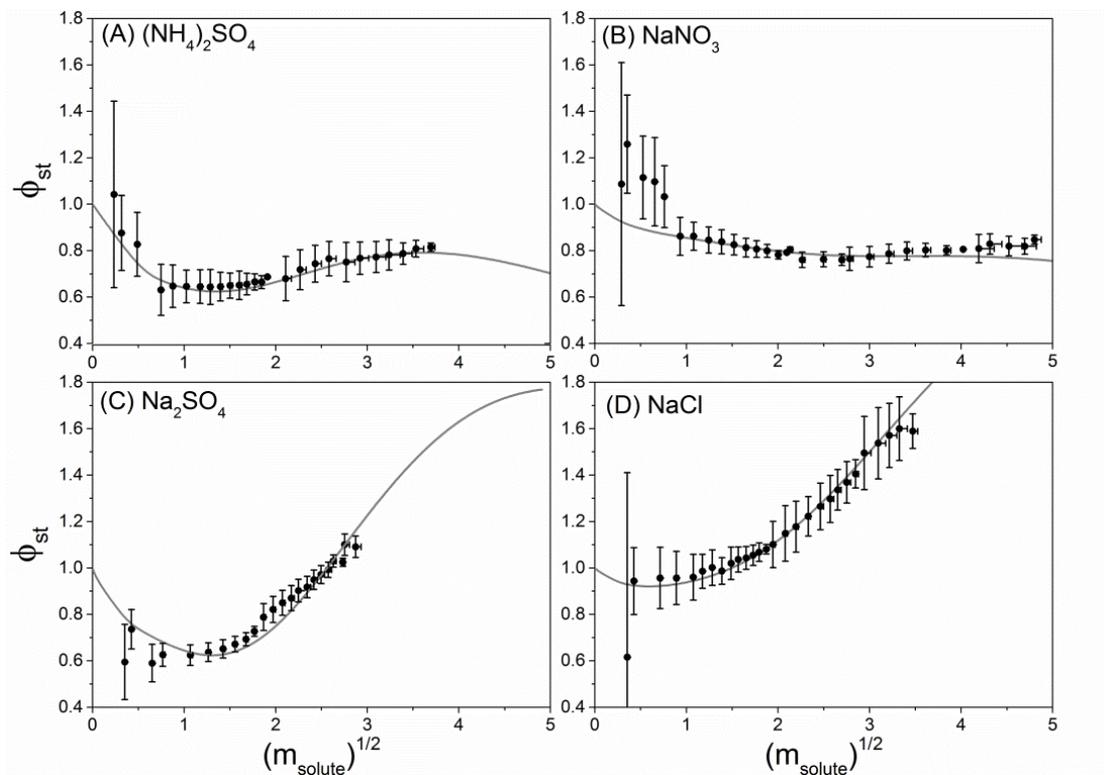
Figure 7. Correlation plot showing the experimentally measured and E-AIM predicted values for n_{water}/n_{solute}, displayed on a logarithmic scale in the main graph and on a linear scale in the inset. Symbols: green - $(NH_4)_2SO_4$; red – $NaNO_3$; blue – Na_2SO_4; purple – $NaCl$; solid line – 1:1 correlation line; grey envelopes: uncertainty on n_{water}/n_{solute} for $(NH_4)_2SO_4$, corresponding to an error in a_w of ± 0.001 (dark grey) and 0.002 (light grey).
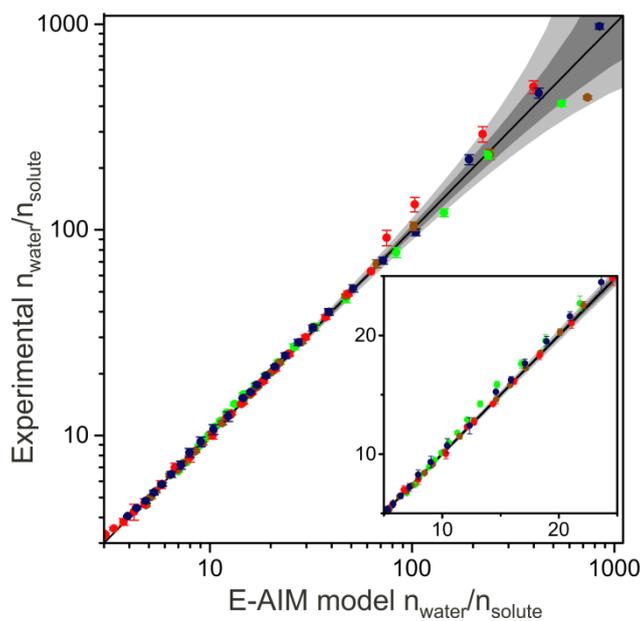
Figure 8. *mfs* vs. a_w (Panel A) and GF_r vs. a_w (Panel B) plots for $(NH_4)_2SO_4$ and NaCl mixtures at different mass ratios, represented in the form $(NH_4)_2SO_4$/NaCl. Symbols: filled circles – experimental data; solid lines – calculations from the E-AIM model for pure $(NH_4)_2SO_4$ and NaCl; dashed lines – calculations from the E-AIM model for the mixtures. From top to bottom in (A) (bottom to top in (B)), the lines/symbols are for pure NaCl (violet), 50/50 ratio (pink), 90/10 ratio (orange), 95/5 ratio (light green), pure $(NH_4)_2SO_4$ (dark green). Note: error bars are smaller than the data point when not shown.
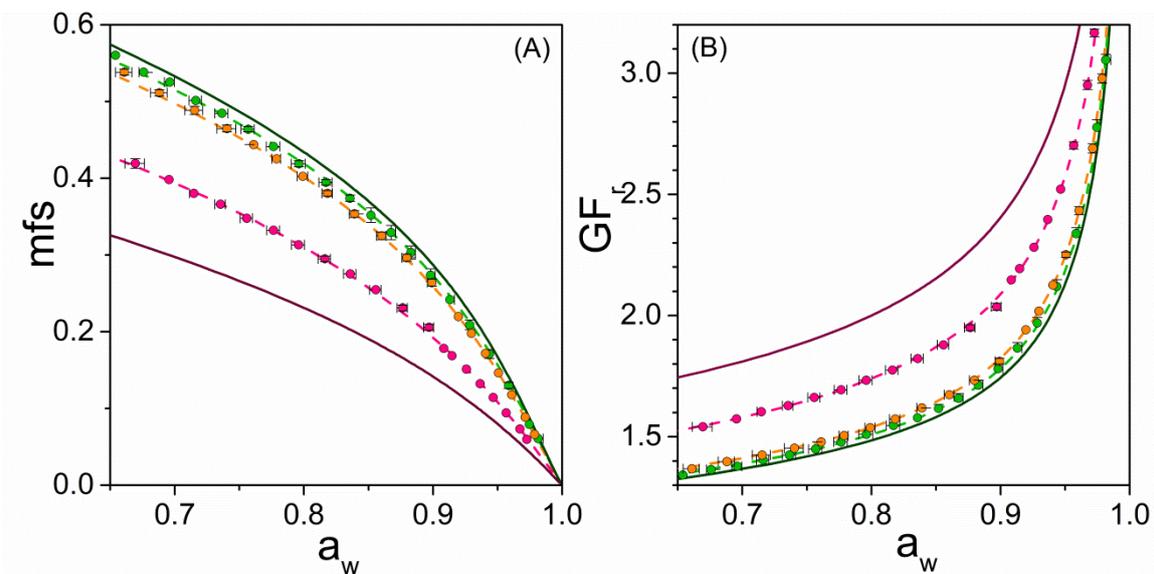
**Figure 9.** n_{water}/n_{solute} vs. a_w growth curve on a logarithmic scale for NaCl obtained when two different values for the mass accommodation coefficient were used in data processing (Equation 5). Symbols: black circles – experimental obtained with $\alpha_M = 1$; open grey circles – experimental obtained with $\alpha_M = 0.1$; solid line – prediction from the E-AIM model.
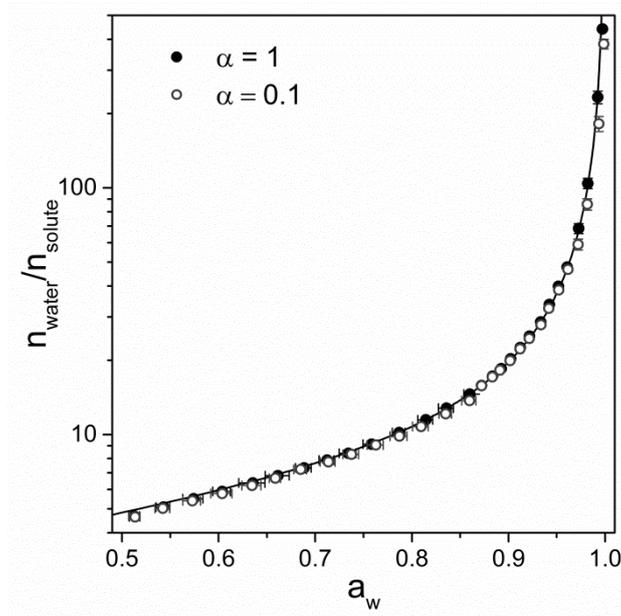
Table of Contents Graphic